Ceramics International xxx (xxxx) xxx–xxx

Contents lists available at ScienceDirect

Ceramics International

journal homepage: www.elsevier.com/locate/ceramint

# Germanium-based complex derived porous $GeO_2$ nanoparticles for building high performance Li-ion batteries

Junhao Zhang[a,b,*], Tingting Yu[a], Jiale Chen[a], Huili Liu[a], Dongqin Su[a], Zehua Tang[a], Jinfeng Xie[a], Lei Chen[a], Aihua Yuan[a,b,*], Qinghong Kong[c]

[a] School of Environmental and Chemical Engineering, Jiangsu University of Science and Technology, Zhenjiang, Jiangsu 212003, China
[b] Marine Equipment and Technology Institute, Jiangsu University of Science and Technology, Zhenjiang, Jiangsu 212003, China
[c] School of the Environment and Safety Engineering, Jiangsu University, Zhenjiang, Jiangsu 212013, China

ARTICLE INFO

*Keywords:*
Thermal decomposition
Porous $GeO_2$ nanoparticles
Anode material
Long cycle life
Lithium storage performance

ABSTRACT

Germanium-based materials possess promising potential as novel anode materials for high performance lithium-ion batteries (LIBs). However, the considerably huge volume change causes rapid capacity fade during the charge-discharge process. A simple strategy was devised to prepare porous $GeO_2$ nanoparticles via thermal decomposition of $(Hbipy)_2[Ge(C_2O_4)_3]\cdot 2H_2O$ in air atmosphere. As an anode material for LIBs, it shows superior electrochemical performance in comparison with commercial $GeO_2$ microparticles. The initial discharge capacity of porous $GeO_2$ nanoparticles is high to 2578.8 mA h/g, and it still retained 581.9 mA h/g after 100 cycles. Even at 2 A/g, a reversible discharge capacity of 184.2 mA h/g is yet obtained. The superior lithium storage performances should be chalked up to the positive synergism of nanoscale, porous structure and low crystalline nature, which effectively retard the huge volume change of $GeO_2$ and are beneficial for fast diffusion of lithium ions during cycling.

## 1. Introduction

Nowadays, the disadvantages of LIBs are narrow operating temperature range and low energy density [1]. Currently, fully charged electric vehicles using LIBs is only power to run up to 150 kilometers, which can't meet the requirement of much high energy/power density [2]. Consequently, many work focused on increasing the specific capacity to elevate the energy density of the anode materials in LIBs [3–5].

Recently, metal oxides with nanostructures [6–12], such as $SnO_2$, $V_2O_5$, $MnO_2$, are extensively studied based on the high theoretical specific capacities and volume energy densities compared with graphite anode materials for LIBs. However, they can't fully satisfy the energy density requirements for high-performance LIBs because of relatively low conductivity and poor rate capability. Several materials with higher Li storage capacity are good candidate anode materials, such as Si and Ge [13,14]. Compared with Si anode material, Ge rarely gets attention owing to its higher cost. Nonetheless, it has merits on better lithium diffusion and higher electronic conductivity. Some groups have devoted to Ge-based materials with different structures that are considered as an alternative to commercial graphite owing to the high theoretical capacities (such as 1623 mA h/g for Ge anode material) and faster charge transfer properties [15–17]. The $GeO_x$ is also an attractive candidate, and $GeO_2$ is able to deliver the specific capacity of 2152 mA h/g if it stores 8.4 $Li^+$ reversibly. $GeO_2$ has some other advantages over pure Ge, such as lower cost, better chemical and cyclical stability [18].

It's well known that most of the $GeO_2$ anodes are afflicted with poor cycling life, which is a tough conundrum for $GeO_2$ anodes. Similar to alloy anodes, $GeO_2$ anodes are afflicted with large volume expansion in charge-discharge processes, causing pulverization of $GeO_2$ and instability solid electrolyte interface (SEI) [19,20]. Numerous efforts have been focused on exploring for addressing this issue, such as hybridization, reducing size, amorphization and rational fabrication of nanostructures [21–28]. Recently, the common strategy is devoted to hybridization of $GeO_2$ material with carbonaceous materials. Carbon as buffer layer will reduce the weight content of $GeO_2$ material in the electrode, thus the specific capacity of the total material will be reduced partly. Small particle size can alleviate the pulverization of $GeO_2$ particles, but also reduce the diffusion path of $Li^+$, thereby improving the lithium storage performance. Porous structures can well relax the mechanical strain from huge volume expansion during cyclic process, and exhibit large surface area that increases electrode-electrolyte interface, and have nanometer thick walls, which are beneficial for fast diffusion of $Li^+$. Nevertheless, the controllable preparation of porous $GeO_2$

* Corresponding authors at: School of Environmental and Chemical Engineering, Jiangsu University of Science and Technology, Zhenjiang, Jiangsu 212003, China.
*E-mail addresses:* jhzhang6@just.edu.cn (J. Zhang), aihua.yuan@just.edu.cn (A. Yuan).

http://dx.doi.org/10.1016/j.ceramint.2017.10.069
Received 23 September 2017; Received in revised form 11 October 2017; Accepted 11 October 2017

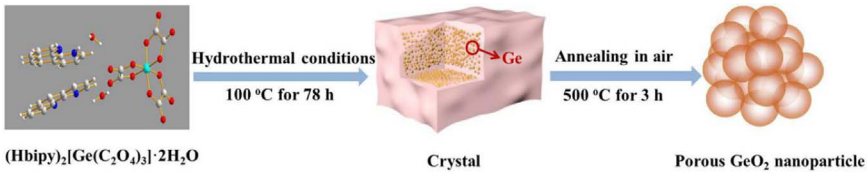


**Fig. 1.** Schematic preparation route of porous $GeO_2$ nanoparticles.

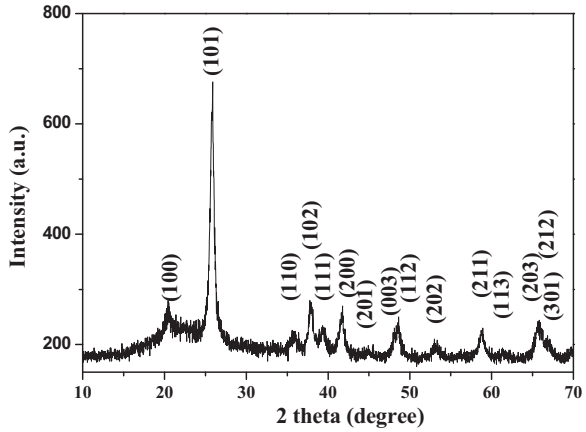


**Fig. 2.** XRD pattern of $GeO_2$ nanoparticles through thermolysis of germanium precursor at 500 °C for 3 h.

nanostructures is urgent but challenging as a result of the lack of efficient synthetic methods.

Here, a simple and novel strategy was proposed to fabricate porous $GeO_2$ nanoparticles by annealing $(Hbipy)_2[Ge(C_2O_4)_3]\cdot 2H_2O$ under air atmosphere, which have the merits of excellent cycling performance, environmental friendliness, and simple manufacturing process. The porous $GeO_2$ nanoparticles with mesoporous structure was synthesized firstly, and have an increased surface area compared with commercial $GeO_2$ microparticles, which provides an effective buffering environment to alleviate the huge volumetric expansion of $GeO_2$ nanoparticles in the cycle process. The porous $GeO_2$ nanoparticles exhibit excellent reversible capacity and rate capacity as an anode material for LIBs. Therefore, the simple method promotes the tremendous potential of germanium based anodes for further spread applications. Meanwhile, these nanomaterials will be more widely used in other intelligent energy storage devices in the future [29–32].

## 2. Experimental section

2, 2′-bipyridine was purchased from Aladdin Chemical Co. Polyethylene glycol-2000 (PEG-2000, analytical grade) was obtained from J·K Reagent Co. Ltd (China). Oxalic acid ($H_2C_2O_4\cdot 2H_2O$, ≧ 99.0%) and germanium dioxide ($GeO_2$, ≧ 99.99%, ≥ 200 mesh) were from Sinopharm Chemical Reagent Co., Ltd.

### 2.1. Synthesis of $(Hbipy)_2[Ge(C_2O_4)_3]\cdot 2H_2O$ precursor

Firstly, 1.0 mmol of commercial $GeO_2$ microparticles, 3.0 mmol of $H_2C_2O_4\cdot 2H_2O$, 1 mmol PEG-2000 and 2.0 mmol 2, 2′-bipyridine were added into 15 mL deionized water. Subsequently, the mixture was agitated vigorously to form homogeneous suspension, which was transferred to a Teflon autoclave, sealed and put into an air dry oven at room temperature, and the furnace temperature was increased to 100 °C and maintained for 78 h. After the autoclave cooling down naturally, the solid precipitate was collected and washed by distilled water and air-dried under room conditions.

### 2.2. Preparation of porous $GeO_2$ nanoparticles

The Ge-based complex precursor was transferred into the pipe furnace followed by annealing at 400, 500, 600, 800 °C under air for 3 h to prepare $GeO_2$ nanoparticles with different crystallinity and size.

### 2.3. Characterization

Single crystal X-ray diffraction (SXRD) studies for Ge-based complex precursor were carried out on a Bruker SMART APEX Π with graphite-monochromatic Mo Kα radiation (λ = 0.71073 Å). Data processing including empirical adsorption correction was performed using SADABS. Thermal stability was investigated using a Mettler Toledo TGA/SDTA851 thermal analyzer in $O_2$ atmosphere with a heating rate of 10 °C $min^{-1}$. The morphologies and detailed structures of the products were observed by field emission scanning electron microscopy (FESEM, ZEISS Merlin Compact), transmission electron microscopy (TEM, JEOL JEM-2100F, 20 kV). The elemental mappings were obtained using the energy dispersive spectroscopy (EDS, Oxford X-Max). The phase and composition of $GeO_2$ nanoparticles were investigated by power X-ray diffraction (XRD, Shimadzu XRD-6000) with Cu-Kα radiation (0.15406 nm). $N_2$ adsorption-desorption isotherms of the samples were conducted at 77 K in a Micromerities ASAP 2020 instrument. The surface electronic states were studied by X-ray photoelectron spectroscopy (XPS, Thermo Fisher Scientific Escalab-250Xi using Al-Kα radiation).

### 2.4. Electrochemical measurements

The lithium storage performance was evaluated via a coin-type half cells (CR2032) using the porous $GeO_2$ nanoparticles as working electrode, which was made up by blending porous $GeO_2$ nanoparticles (80 wt%), polyvinylidene fluoride (10 wt%) and acetylene black (10 wt %), and was dispersed in N-methyl pyrrolidone, uniformly overlayed on copper foil and then dried in a vacuum box at 85 °C overnight. $LiPF_6$ was dissolved in mixed solvents (1:1 v/v) of ethylene carbonate and dimethyl carbonate to form 1 mol $L^{-1}$ solution as electrolyte. Li foil and Celgard 2400 micro-porous film were served as the counter electrode and separator. Cyclic voltammetry (CV) test was performed on a CHI660D electrochemical workstation between 0.01 and 3.0 V at 0.2 mV $s^{-1}$. Galvanostatic charge-discharge cycles were measured on a battery tester (LAND CT 2001A). Electrochemical impedance spectroscopy (SEI) was assessed with frequency range from 100 kHz to 10 mHz.

## 3. Results and discussion

Fig. 1 presents schematic preparation route of porous $GeO_2$ nanoparticles, which was mainly based on the complex and thermal decomposition of germanium precursor using $GeO_2$ as Ge source and oxalic acid as coordination agent in the presence of 2, 2′-bipyridine, which can promote the growth and stabilization of germanium complex. Additionally, PEG-2000 as surfactant can promote the dispersion of $GeO_2$ particles in solvent [33–38]. Commercial $GeO_2$ microparticles with low cost were used, which size was about several micrometers and the surface of microparticles was rough, shown in Fig. S1. Fig. S2a shows that the appearance of germanium precursor is cuboid with the length of 35 μm. The crystal structure of the germanium precursor was

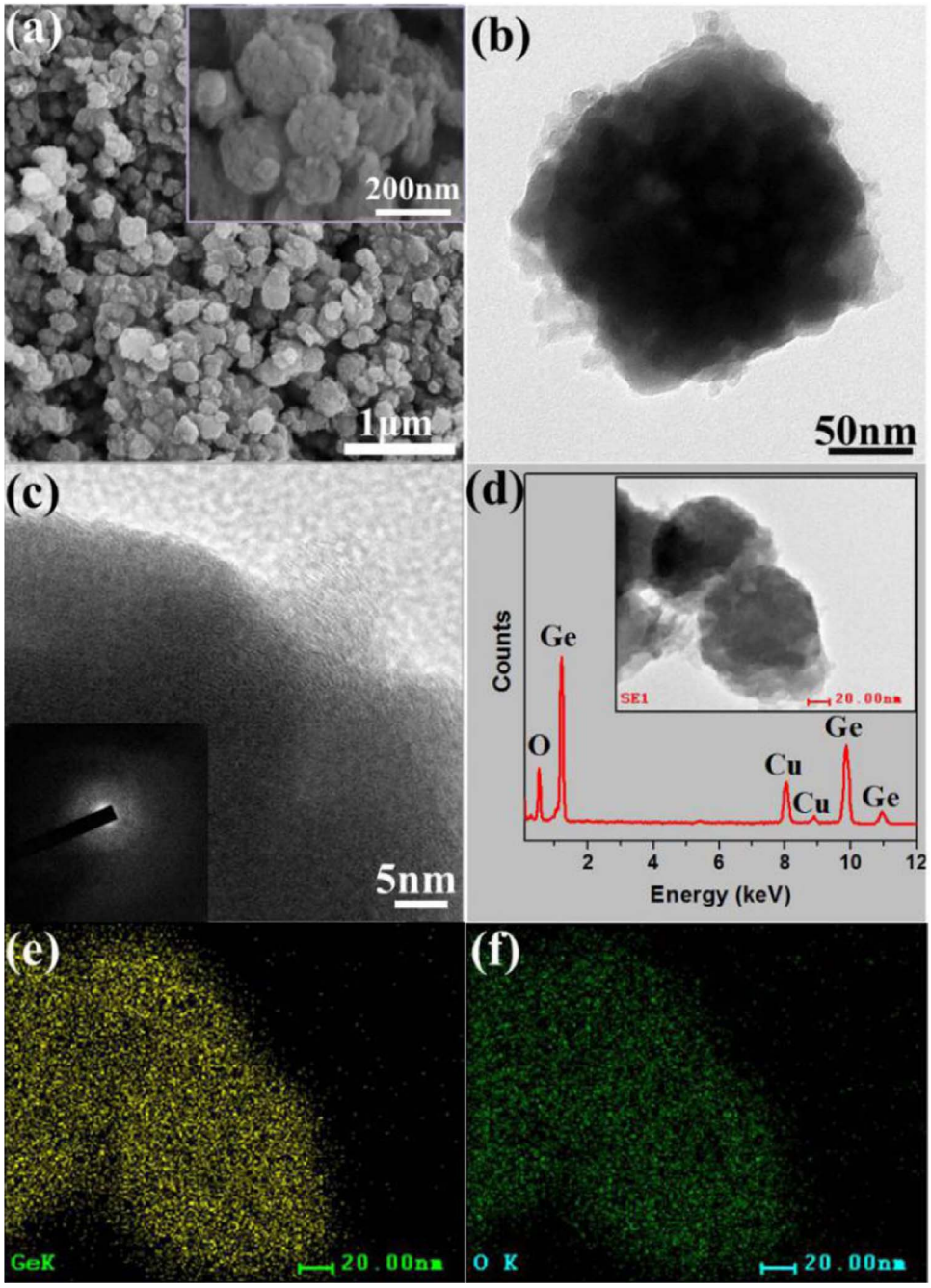


**Fig. 3.** (a) FESEM images of the product obtained at 500 °C; (b) TEM image of single porous $GeO_2$ nanoparticle; (c) HRTEM image and SAED pattern (inset) of porous $GeO_2$ nanoparticles; (d) EDS and the corresponding TEM image of the porous $GeO_2$ nanoparticles; (e) elemental mapping of Ge; (f) elemental mapping of O.

affirmed by SXRD, and Crystal data for the germanium precursor are consistent with those of the previous report [39]. Structure schematic drawing has been made by the software package crystal diamond, which indicated that the complex is $(Hbipy)_2[Ge(C_2O_4)_3]\cdot 2H_2O$, as shown in Fig. S2b. Fig. 2c is FTIR spectroscopy of the germanium precursor. Selected FTIR data (in $cm^{-1}$): $\nu$(N-H) = 3211w; $\nu_{sym}$(C-H) = 3106m, 3055, 2955w; $\nu$(C=O) = 1746s; $\nu_{asym}(-CO_2^-)$ = 1674m, 1591m, 1529m; $\nu_{sym}(-CO_2^-)$ = 1470m, 1437m, 1330s; $\nu$(C–O) = 1233m, 1184m; $\nu$(C–H) = 1089w, 992w, 953w, 895m; $\gamma$(C–H) = 609m; $\rho$[(C=O)–O] = 471m, 439w. The thermal stability of the precursor was performed by TGA under air atmosphere, as shown in Fig. S2d. The thermal degradation includes two steps from 248 °C to 335 °C. The first one occurs between 246 °C and 275 °C with the weight loss of 38.1%, which is from the removal of 2, 2′-bipyridine and partial oxalic acid. The second weight loss of 45.2% between 300 °C and 335 °C could be ascribed to the oxidation of oxalic acid. The total loss (83.3%) consists with the calculated value (83.9%) of the exhaustive decomposition of organic fraction and formation of $GeO_2$ with corresponding stoichiometric ratio. Based on the result of TG, the complex was decomposed at 400, 500, 600 and 800 °C for 3 h in air, and the obtained $GeO_2$ nanoparticles were assembled to coin-type half cells to study the electrochemical performances for LIBs as anode material.

Fig. 2 is a XRD pattern of obtained product at 500 °C. The result indicates that the diffraction pattern can be indexed to hexagonal $GeO_2$ (PDF # 36-1463), and no impurity peaks are observed, suggesting germanium precursor has been completely transformed into $GeO_2$. Combining with the above result, Fig. S3 illuminate that the diffraction peak intensity of $GeO_2$ is increased continually with increasing the annealing temperature, indicating the crystallinity was affected by the decomposition temperature. Fig. 3a is the FESEM image of $GeO_2$ obtained at 500 °C, displaying that the uniform $GeO_2$ nanoparticles are assembled by smaller nanoparticles, and the $GeO_2$ nanoparticles is

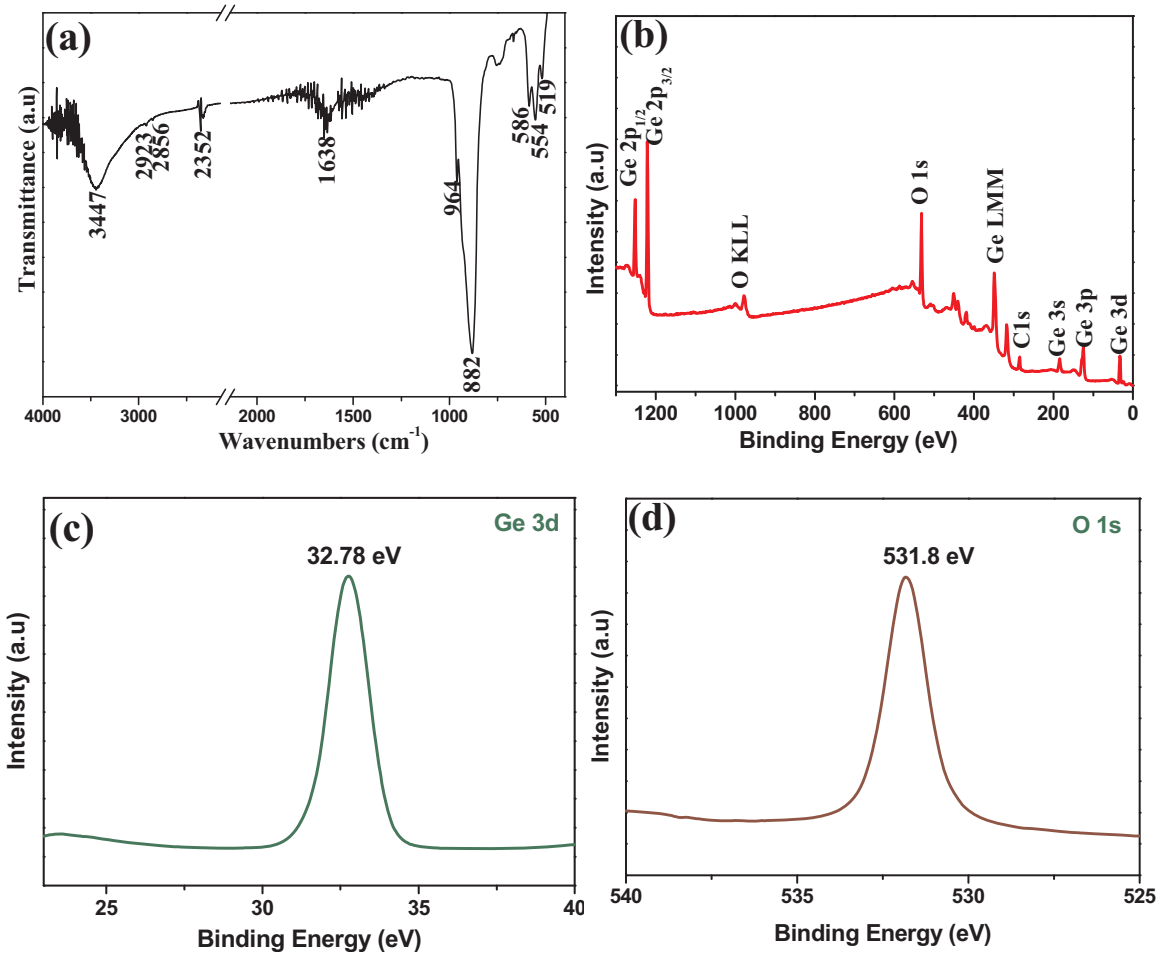


**Fig. 4.** (a) FT-IR spectra of the porous $GeO_2$ nanoparticles; (b-d) XPS spectrum of the porous $GeO_2$ nanoparticles: (b) a wide scan spectrum; (c) a spectrum of Ge3d; (d) a spectrum of O1s.

about 200 nm in Fig. 3b. The FESEM image in Fig. S4a displays that the $GeO_2$ nanoparticles obtained at 400 °C have the diameter of about 600 nm and there are some smaller nanoparticles on the surface of particles from Fig. S4b. When the decomposition temperature is risen to 600 °C, the products in Fig. S4c are a large number of irregular particles, and Fig. S4d shows that the size of particles is further reduced to less than 100 nm. When the decomposition temperature is further risen to 800 °C, the FESEM images of $GeO_2$ are presented in Fig. 3f, which show that the products are irregular and nonuniform particles, and Fig. S4e shows that the size of most particles is more than 400 nm.

The porous $GeO_2$ nanoparticles at 500 °C was selected and further investigated through TEM, HRTEM, selected area electron diffraction (SAED) and element analysis. The TEM image of $GeO_2$ nanoparticle (Fig. 3b) reflects a similar particle size with the SEM characterization. Meanwhile, it is clearly observed that the as-obtained $GeO_2$ nanoparticle at 500 °C has mesoporosity. Fig. 3c shows a HRTEM image, revealing that no clear lattice spacing is observed, indicating its low crystalline nature [16]. The diffuse scattering SAED pattern (inset in Fig. 3c) also reveals the obtained $GeO_2$ with low crystalline structure, which agrees with the results of HRTEM image. Besides, Fig. 3d-f show the EDS, TEM and elemental mapping images of porous $GeO_2$ nanoparticles, which reveal the existence of Ge and O, wherein Cu is from copper grid. The elemental mapping images in Fig. 3e and f show a highly uniform distribution of Ge and O. More interestingly, the two elements are overlapped uniformly across the whole particles, revealing the homogeneous distribution of Ge and O in the porous $GeO_2$ nanoparticles.

The structure of porous $GeO_2$ nanoparticles was further studied through FTIR spectrum. In Fig. 4a, the bands at 519, 554, 586, 882 and 964 $cm^{-1}$ correspond to six characteristic stretching vibration of α-$GeO_2$, which always appear at higher wave number, suggesting the low crystalline of the porous $GeO_2$ nanoparticles, in agreement with XRD results. The peaks at 1638, 2352, 2856, 2923 and 3447 $cm^{-1}$ are from $H_2O$ and $CO_2$, which are introduced in the synthesis process [40]. The above characterizations clarify that the sample is pure $GeO_2$ nanoparticles. Meanwhile, the surface composition of $GeO_2$ was further studied by XPS in Fig. 4(b-d). A wide scan spectrum is displayed in Fig. 4b, the peaks correspond to C 1s, O 2s, 1s and Ge (3d, 3p, 3s, 2p), and O KLL and Ge LMM Auger peaks are also observed. The peaks of Ge 3d and O 1s are observed at 32.78 and 531.8 eV, as shown in Fig. 4c and d, declaring that O and Ge elements exist in $O^{2-}$ and $Ge^{4+}$ oxidation state, respectively.

The surface structure has a significant effect for lithium storage performances of electrode active materials. The adsorption-desorption isotherm of the porous $GeO_2$ nanoparticles in Fig. 5a is the type IV profile with an obvious adsorption-desorption loop at $P/P_0$ of 0.83–0.99, suggesting that the products are mesoporous structure [14]. Fig. 5b is the pore size distribution that the mesoporous with broad pore size distribution is centered between 2.5 and 12 nm. The porous $GeO_2$ nanoparticles exhibit bigger BET surface area of 74.0 $m^2/g$ and large total pore volume of 0.208 $cm^3/g$. In contrast, the commercial $GeO_2$ microparticles only exhibit a BET surface area of 33.6 $m^2/g$ and a total pore volume of 0.041 $cm^3/g$ (Fig. 5c) and no mesopores exist (Fig. 5d). The large surface area and suitable pore size provide more active sites and insure an efficient transportation pathway between electrode materials and electrolyte [41]. The mesoporous structure inside the porous $GeO_2$ nanoparticles also facilitate to alleviate the volume expansion and improve the energy storage performance.

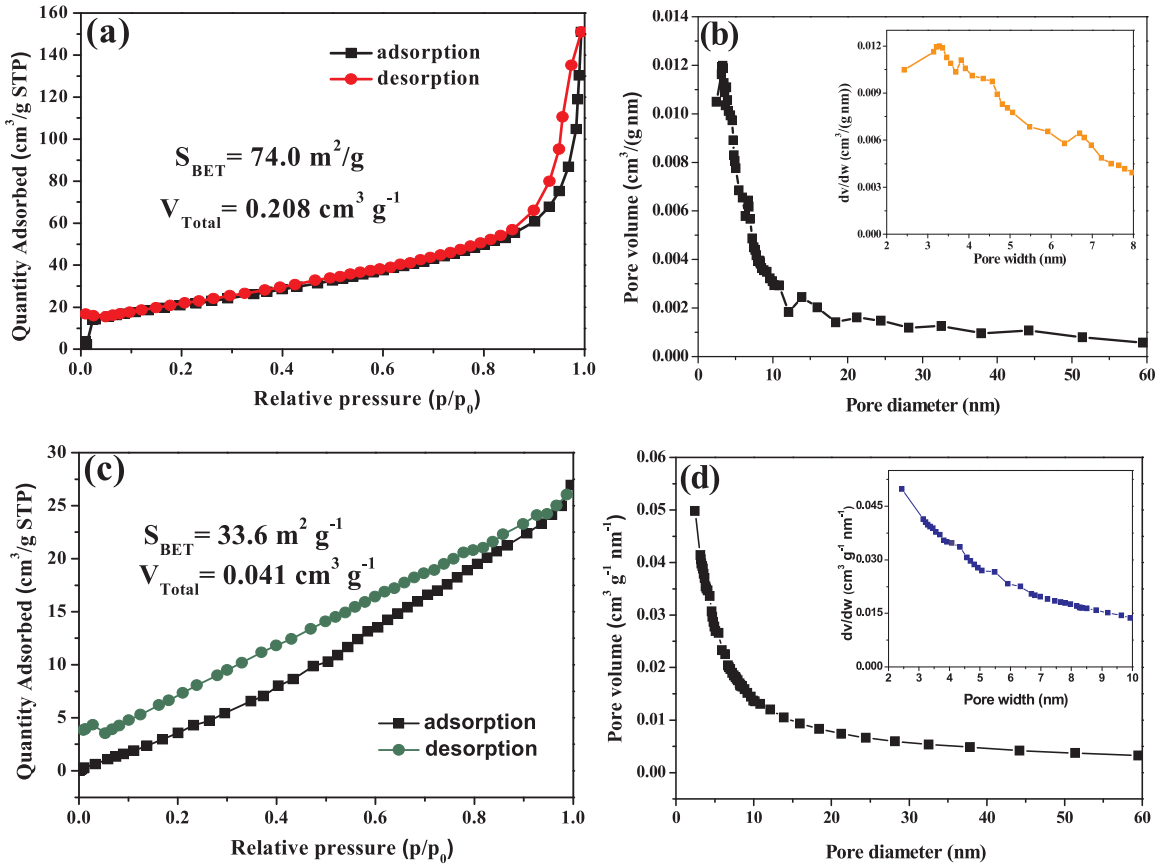


**Fig. 5.** (a) $N_2$ adsorption-desorption isotherm of porous $GeO_2$ nanoparticles; (b) Pore size distribution of porous $GeO_2$ nanoparticles; (c) $N_2$ adsorption-desorption isotherm of commercial $GeO_2$ microparticles; (d) Pore size distribution of commercial $GeO_2$ microparticles.

Considering that the porous $GeO_2$ nanoparticles have some favorable features as LIB anode materials, such as porous structure, nanoscale, higher BET surface area and larger pore volume, the lithium storage performances were tested in 2032 coin-type half-cells at 25 °C. Fig. 6a is the 1st and 2nd cycle voltage profiles of the porous $GeO_2$ nanoparticles at 100 mA/g. Initial discharge and charge capacities are about 2578.8 and 1624 mA h/g, and Coulombic efficiency is about 62.97%. Significantly, the 1st discharge capacity is larger than the theoretical capacity (2152 mA h/g), and the reason should be the formation of SEI layer on the surface of $GeO_2$ active material and reoxidation [42]. The large capacity loss in the 2nd cycle can be ascribed to the irreversible reaction of $GeO_2$ during the Li insertion process by formation of $Li_2O$ [43]. It's well known that improving rate capability is a very important task for anode materials used in electric vehicles [44]. Fig. 6b presents the 1st discharge/charge curves of the porous $GeO_2$ nanoparticle anode at various rates of 100–2000 mA/g, which exhibit that the porous $GeO_2$ nanoparticles have a fairly good rate capability. Even the current density is high to 2000 mA/g, the porous $GeO_2$ nanoparticles still maintains a reversible discharge capacity of 184.2 mA h/g. Fig. 6c displays the remarkable rate capability of porous $GeO_2$ nanoparticle anode, and the charge capacity is 968, 579, 398, 283, 161 mA h/g at different current densities from 100 to 2000 mA/g. Importantly, after high-rate measurements of 2000 mA/g, the specific capacity reversibly recovers to 727 mA h/g once it is restored to 100 mA/g, declaring excellent electrochemical reversibility and structure stability. Fig. 6d presents the cycling performances of the commercial $GeO_2$ and porous $GeO_2$ nanoparticles at 100 mA/g. The results show that the specific capacity of commercial $GeO_2$ microparticles fast decline to 256.5 mA h/g, and present a capacity retention of 12.1% after 100 cycles. In contrast, the porous $GeO_2$ nanoparticles exhibit a stable capacity of 1349 mA h/g up to the 5th cycle, and fades decreasingly to 581.9 mA h/g after 100 cycles. The mesoporous in porous $GeO_2$ nanoparticles could effeciently alleviate the volumetric change in circle process, and be propitious to electrolyte penetration and electron transfer [45,46].

The lithium storage mechanism of porous $GeO_2$ nanoparticles was investigated using CV and EIS, and the results are shown in Fig. 7. Three CV cycles in Fig. 7a were tested for the porous $GeO_2$ nanoparticles at 0.2 mV $s^{-1}$. A distinct reduction peak at ~ 0.41 V in the first cathodic scan, shifting to ~ 0.38 V in the following cycles, which is in connection with the production of non-crystalline $Li_xGeO_2$ [47]. The peak at about 0.23 V in the 2nd cycle is ascribed to the formation of SEI. With the charge and discharge, the peaks gradually die down and disappear, indicating cycle performance will be stabilization. The peak at ~ 0.05 V owns to Li-Ge alloying reaction [48]. In the anodic scan process, the broad peak at ~ 0.58 V corresponds to dealloying of $Li_xGe$ and oxidation of Ge. The obvious peak at ~ 1.24 V has been confirmed to be reoxidation of Ge to $GeO_2$, leading to be higher capacity than that of commercial $GeO_2$ [44]. Nyquist plots of commercial $GeO_2$ microparticles and porous $GeO_2$ nanoparticles are provided in Fig. 7b. The semicircle in high-frequency region is attributed to charge transfer resistance and $Li^+$ migration through the electrolyte interface, which in this case take place at the similar intermediate frequencies. At the low frequencies the straight line manifests a combination of electrolyte diffusion and slow changes in the active film due to the lithiation [49,50]. As a result, the porous $GeO_2$ nanoparticle electrode exhibited smaller charge transfer resistance than commercial $GeO_2$ microparticles, suggesting that the porous $GeO_2$ nanoparticles can short diffusion pathway for electron and electrolyte ion, promote the electrolyte to penetrate into electrode material, and improve the diffusion efficiency of $Li^+$ ions.

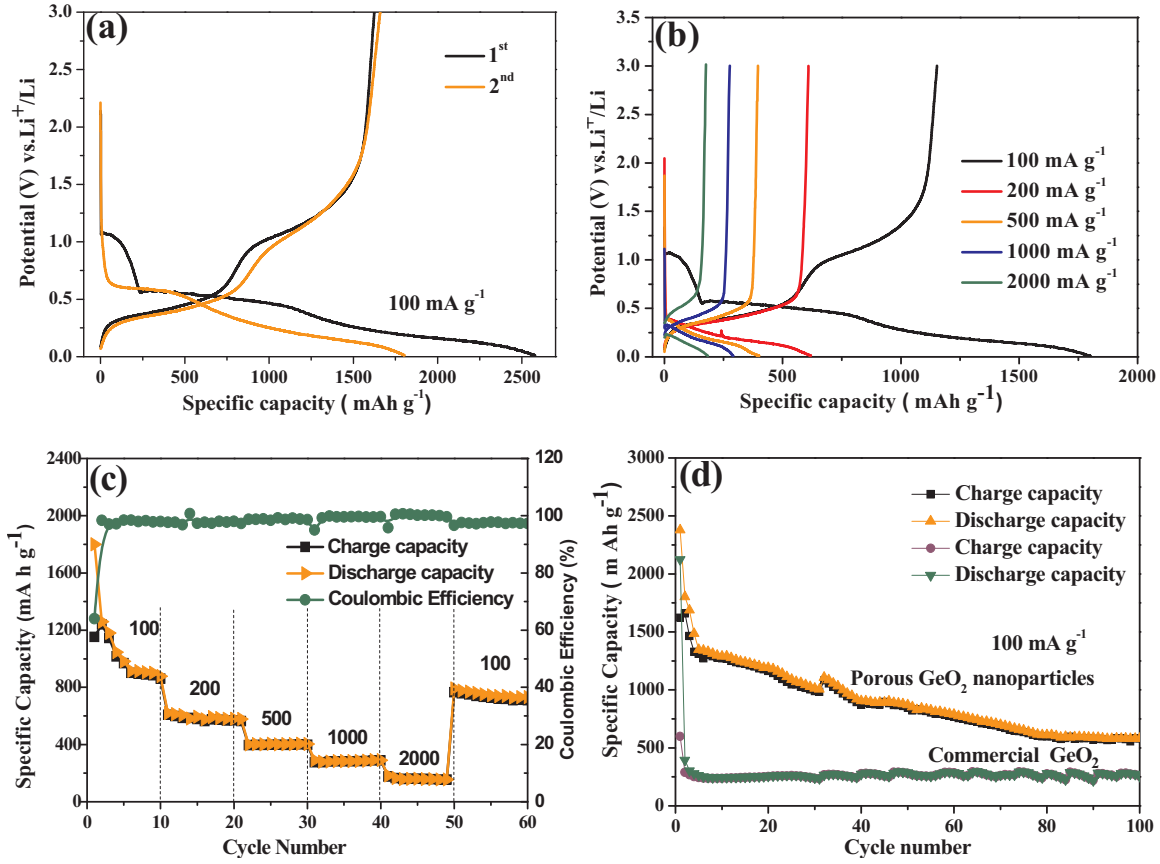


**Fig. 6.** Electrochemical performances of the porous $GeO_2$ nanoparticle electrode: (a) Charge/discharge curves at 1st and 2nd cycle; (b) Initial charge-discharge curves at different current densities; (c) Rate capability under different charge-discharge rate for each 10 cycles; (d) Cycle performance.

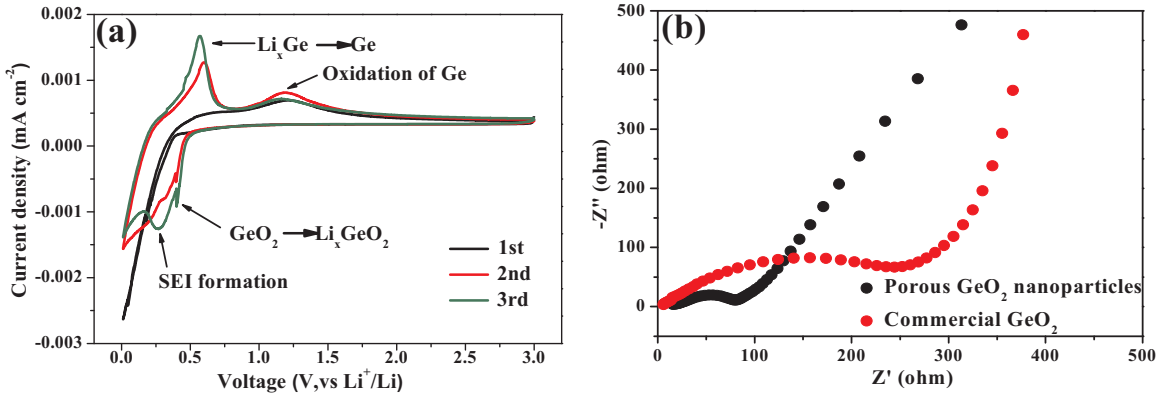


**Fig. 7.** (a) CV curves of the porous $GeO_2$ nanoparticles; (b) EIS of commercial $GeO_2$ microparticles and porous $GeO_2$ nanoparticles.

## 4. Conclusions

In summary, $GeO_2$ nanoparticles was devised and prepared via annealing $(Hbipy)_2[Ge(C_2O_4)_3]\cdot 2H_2O$ precursor in air atmosphere. The obtained porous $GeO_2$ nanoparticles at 500 °C showed average size with 200 nm, mesoporous with 4 nm, BET surface area with 74.0 $m^2/g$ and total pore volume with 0.208 $cm^3/g$, which could mitigate the pulverization of the electrode materials and reduce the diffuse route of $Li^+$, elevating electrochemical performance. Serving as an anode for LIBs, the $GeO_2$ nanoparticles with mesoporous structure displayed a high discharge capacity of 2578.8 mA h/g at 100 mA/g. Excellent reversible capacity of 581.9 mA h/g for lithium storage was obtained after 100 cycles. Even at 2 A/g, it still retained a capacity of 184.2 mA h/g. Our facile strategy can successfully address the current challenge of controllable synthesis of $GeO_2$ nanostructures, and this strategy can also be applied to controllably prepare other metal oxides.

## Acknowledgments

The study was financially supported by the National Natural Science of Foundation of China (Nos. 51672114, 51603091), the China Postdoctoral Science Foundation (No. 2017M611747), Foundation from Marine Equipment and Technology Institute for Jiangsu University of Science and Technology (No. HZ20170015), and Qinglan Project of Jiangsu Province.

## Appendix A. Supporting information

Supplementary data associated with this article can be found in the online version at http://dx.doi.org/10.1016/j.ceramint.2017.10.069.

## References

[1] J.H. Lee, C.S. Yoon, J.Y. Hwang, S.J. Kim, F. Maglia, P. Lamp, S.T. Myung, Y.K. Sun, High-energy-density lithium-ion battery using a carbon-nanotube-Si composite anode and a compositionally graded $Li[Ni_{0.85}Co_{0.05}Mn_{0.10}]O_2$ cathode, Energy Environ. Sci. 9 (2016) 2152–2158.

[2] M.M. Rahman, I. Sultana, T.Y. Yang, Z.Q. Chen, N. Sharma, A.M. Glushenkov, Y. Chen, Lithium germanate ($Li_2GeO_3$): a high-performance anode material for lithium-ion batteries, Angew. Chem. Int. Ed. 55 (2016) 16059–16063.

[3] K.S. Eom, J.T. Lee, M. Oschatz, F.X. Wu, S. Kaskel, G. Yushin, T.F. Fuller, A stable lithiated silicon-chalcogen battery via synergetic chemical coupling between silicon and selenium, Nat. Commun. 8 (2017) 13888.

[4] J.H. Zhang, M. Huang, B.J. Xi, K. Mi, A.H. Yuan, S.L. Xiong, Systematic study of effect on enhancing specific capacity and electrochemical behaviors of lithium-sulfur batteries, Adv. Energy Mater. (2017), http://dx.doi.org/10.1002/aenm.201701330.

[5] Y.Y. Chen, Y. Wang, H.X. Yang, H. Gan, X.W. Cai, X.M. Guo, B. Xu, M.F. Lü, A.H. Yuan, Facile synthesis of porous hollow $Co_3O_4$ microfibers derived-from metal-organic frameworks as an advanced anode for lithium ion batteries, Ceram. Int. 43 (2017) 9945–9950.

[6] W.J. Dong, J.J. Xu, C. Wang, Y. Lu, X.Y. Liu, X. Wang, X.T. Yuan, Z. Wang, T.Q. Lin, M.L. Sui, I.W. Chen, F.Q. Huang, A robust and conductive black tin oxide nanostructure makes efficient lithium-ion batteries possible, Adv. Mater. 29 (2017) 1700136.

[7] Y. Yue, H. Liang, Mirco-and nano-structured vanadium pentoxide ($V_2O_5$) for electrodes of lithium-ion batteries, Adv. Energy Mater. 7 (2017) 1602545.

[8] S. Deng, L. Wang, T. Hou, Y.Y. L, Two-dimensional $MnO_2$ as a better cathode material for lithium ion batteries, J. Phys. Chem. C 119 (2015) 28783–28788.

[9] Z.Y. Sun, L. Zhang, F. Dang, Y. Liu, Z.Y. Fei, Q. Shao, H. Lin, H.J. Guo, L.C. Xiang, N. Yerra, Z.H. Guo, Experimental and simulation-based understanding of morphology controlled barium titanate nanoparticles under co-adsorption of surfactants, CrystEngComm 19 (2017) 3288–3298.

[10] L. Zhang, W. Yu, C. Han, J. Guo, Q.H. Zhang, H.Y. Xie, Q. Shao, Z.G. Sun, Z.H. Guo, Large scaled synthesis of heterostructured electrospun $TiO_2/SnO_2$ nanofibers with an enhanced photocatalytic activity, J. Electrochem. Soc. 164 (2017) H651–H656.

[11] C.B. Cheng, R.H. Fan, Z.Y. Wang, Q. Shao, X.K. Guo, P.T. Xie, Y.S. Yin, Y.L. Zhang, L.Q. An, Y.H. Lei, J.E. Ryu, A. Shankar, Z.H. Guo, Tunable and weakly negative permittivity in carbon/silicon nitride composites with different carbonizing temperatures, Carbon (2017), http://dx.doi.org/10.1016/j.carbon.2017.09.037.

[12] X.M. Lou, C.F. Lin, Q. Luo, J.B. Zhao, B. Wang, J.B. Li, Q. Shao, X.K. Guo, N. Wang, Z.H. Guo, Crystal structure modification enhanced $FeNb_{11}O_{29}$ anodes for lithium-ion batteries, ChemElectroChem (2017), http://dx.doi.org/10.1002/celc.201700816.

[13] X. Su, Q.L. Wu, J.C. Li, X.C. Xiao, A. Lott, W.Q. Lu, B.W. Sheldon, J. Wu, Silicon-based nanomaterials for lithium-ion batteries: a review, Adv. Energy Mater. 4 (2014) 1300882.

[14] S. Choi, Y. Cho, J. Kim, N. Choi, H. Song, G.X. Wang, S. Park, Mesoporous germanium anode materials for lithium-ion battery with exceptional cycling stability in wide temperature range, Small 13 (2017) 201603045.

[15] L.X. Zeng, X.X. Huang, X. Chen, C. Zheng, Q.R. Qian, Q.H. Chen, M.D. Wei, Ge/$GeO_2$-ordered mesoporous carbon nanocomposite for rechargeable lithium-ion batteries with a long-term cycling performance, ACS Appl. Mater. Interfaces 8 (2016) 232–239.

[16] W. Wei, F. Jia, P. Qu, Z. Huang, H. Wang, L. Guo, Morphology memory but reconstructing crystal structure: porous hexagonal $GeO_2$ nanorods for rechargeable lithium-ion batteries, Nanoscale 9 (2017) 3961–3968.

[17] F. Zhang, R.H. Zhang, Z. Zhang, H.K. Wang, J.K. Feng, S.L. Xiong, Y.T. Qian, Hydrothermal growth of cobalt germanate/reduced graphene oxide nanocomposite as superior anode materials for lithium-ion batteries, Electrochim. Acta 150 (2014) 211–217.

[18] H.P. Jia, R. Kloepsch, X. He, J.P. Badillo, M. Winter, T. Placke, One-step synthesis of novel mesoporous three dimensional $GeO_2$ and its lithium storage properties, J. Mater. Chem. A 2 (2014) 17545–17550.

[19] S. Yoon, S.H. Jung, K.N. Jung, S.G. Woo, W. Cho, Y.N. Jo, K.Y. Cho, Preparation of nanostructured Ge/$GeO_2$ composite in carbon matrix as an anode material for lithium-ion batteries, Electrochim. Acta 188 (2016) 120–125.

[20] D.T. Ngo, R.S. Kalubarme, T.T. Le, C.N. Park, C.J. Park, Conducting additive-free amorphous $GeO_2$/C composite as a high capacity and long-term stability anode for lithium ion batteries, Nanoscale 7 (2015) 2552–2560.

[21] B. Liu, A. Abouimrane, M. Balasubramanian, Y. Ren, K. Amine, $GeO_2$-SnCoC composite anode Mmaterial for lithium-ion batteries, J. Phys. Chem. C 118 (2014) 3960–3967.

[22] Y. Chen, C.L. Yan, O.G. Schmidt, Strain-driven formation of multilayer graphene/$GeO_2$ tubular nanostructures as high-capacity and very long-life anodes for lithium-ion batteries, Adv. Energy Mater. 3 (2013) 1269–1274.

[23] X.L. Wang, W.Q. Han, H.Y. Chen, J.M. Bai, T.A. Tyson, X.Q. Yu, X.J. Wang, X.Q. Yang, Amorphous hierarchical porous $GeO_x$ as high-capacity anodes for Li ion batteries with very long cycling life, J. Am. Chem. Soc. 133 (2011) 20692–20695.

[24] A.G. Medvedev, A.A. Mildiaylov, D.A. Grishanov, D.Y.W. Yu, J. Gun, S. Sladkevich, O. Lev, P.V. Prikhodchenko, $GeO_2$ Thin film deposition on graphene oxide by the hydrogen peroxide route: evaluation for lithium-ion battery anode, ACS Appl. Mater. Interfaces 9 (2017) 9152–9160.

[25] S.M. Aqeel, Z.Y. Huang, J. Walton, C. Baker, D.L. Falkner, Z. Liu, Z. Wang, Polyvinylidene fluoride (PVDF)/polyacrylonitrile (PAN)/carbon nanotube nanocomposites for energy storage and conversion, Adv. Compos. Hybrid Mater. (2017), http://dx.doi.org/10.1007/s42114-017-0002-5.

[26] G.Q. Yu, Y. Lu, J. Guo, M. Patel, A. Bafana, X.F. Wang, B. Qiu, C. Jeffryes, S.Y. Wei, Z.H. Guo, E.K. Wujcik, Carbon nanotubes, graphene, and their derivatives for heavy metal removal, Adv. Compos. Hybrid. Mater. (2017), http://dx.doi.org/10.1007/s42114-017-0004-3.

[27] K. Zhang, G.H. Li, L.M. Feng, N. Wang, J. Guo, K. Sun, K.X. Yu, J.B. Zeng, T.X. Li, Z.H. Guo, M. Wang, Ultralow percolation threshold and enhanced electromagnetic interference shielding in poly(l-lactide)/multi-walled carbon nanotube nanocomposites with electrically conductive segregated networks, J. Mater. Chem. C 5 (2017) 9359–9369.

[28] T. Liu, K. Yu, L.N. Gao, H. Chen, N. Wang, L.H. Hao, T.X. Li, H.C. He, Z.H. Guo, A graphene quantum dot decorated $SrRuO_3$ mesoporous film as an efficient counter electrode for high-performance dye-sensitized solar cells, J. Mater. Chem. A 5 (2017) 17848–17855.

[29] C. Alippi, A unique timely moment for embedding intelligence in applications, CAAI Trans. Intel. Technol. 1 (2016) 1–3.

[30] H.Y. Jin, Q. Chen, Z.X. Chen, Y. Hu, J.W. Zhang, Multi-leap motion sensor based demonstration for robotic refine tabletop object manipulation task, CAAI Trans. Intel. Technol. 1 (2016) 104–113.

[31] X.Y. Zhang, H.B. Gao, M. Guo, G.P. Li, Y.C. Liu, D.Y. Li, A study on key technologies of unmanned driving, CAAI Trans. Intel. Technol. 1 (2016) 4–13.

[32] S. Padhy, S. Panda, A hybrid stochastic fractal search and pattern search technique based cascade PI-PD controller for automatic generation control of multi-source power systems in presence of plug in electric vehicles, CAAI Trans. Intel. Technol. 2 (2017) 12–25.

[33] K. Sun, P.T. Xie, Z.Y. Wang, T.M. Su, Q. Shao, J. Ryu, X.H. Zhang, J. Guo, A. Shankar, J.F. Li, R.H. Fan, D.P. Cao, Z.H. Guo, Flexible polydimethylsiloxane/multi-walled carbon nanotubes membranous metacomposites with negative permittivity, Polymer 125 (2017) 50–57.

[34] Y.C. Li, X.L. Wu, J.F. Song, J.F. Li, Q. Shao, N. Cao, N. Lu, Z.H. Guo, Reparation of recycled acrylonitrile- butadiene-styrene by pyromellitic dianhydride: reparation performance evaluation and property analysis, Polymer 124 (2017) 41–47.

[35] C. Wang, Y.C. Wu, Y.C. Li, Q. Shao, X.R. Yan, C. Han, Z. Wang, Z. Liu, Z.H. Guo, Flame-retardant rigid polyurethane foam with a phosphorus-nitrogen single intumescent flame retardant, Polym. Adv. Technol. (2017), http://dx.doi.org/10.1002/pat.4105.

[36] W.Q. Yang, X.L. Wang, J.F. Li, X.R. Yan, S.S. Ge, S. Tadakamalla, Z.H. Guo, Polyoxymethylene/ethylene butylacrylate copolymer/ethylene-methyl acrylate-glycidyl methacrylate ternary blends, Polym. Eng. Sci. (2017), http://dx.doi.org/10.1002/pen.24675.

[37] J.N. Huang, Y.H. Cao, Q. Shao, X.F. Peng, Z.H. Guo, Magnetic nanocarbon adsorbents with enhanced hexavalent chromium removal: morphology dependence of fibrillary vs particulate structures, Ind. Eng. Chem. Res. 56 (2017) 10689–10701.

[38] Y.J. Zheng, Y. Zheng, S. Yang, Z.H. Guo, T. Zhang, H.X. Song, Q. Shao, Esterification synthesis of ethyl oleate catalyzed by Brønsted acid-surfactant-combined ionic liquid, Green Chem. Lett. Rev. 10 (2017) 202–209.

[39] L. Cunha-Silva, F.N. Shi, F.A. Almeida Paz, M.J. Hardie, J. Klinowski, T. Trindade, J. Rocha, Supramolecular salts containing the anionic $[Ge(C_2O_4)_3]^{2-}$ complex and heteroaromatic amines, Inorg. Chim. Acta 362 (2009) 263–270.

[40] J.H. Zhang, M. Huang, K. Yanagisawa, S.S. Yao, Y.S. Qiu, H.J. Zheng, Large scale preparation of β-$CaSiO_3$ nanostructures by solid state reaction in NaCl-$H_2O$(v) system at lower temperature, J. Am. Ceram. Soc. 98 (2015) 2264–2268.

[41] M. Huang, K. Mi, J.H. Zhang, H.L. Liu, T.T. Yu, A.H. Yuan, Q.H. Kong, S.L. Xiong, MOFs-derived bi-metal embedded N-doped carbon polyhedral nanocages with enhanced lithium storage, J. Mater. Chem. A 5 (2017) 266–274.

[42] R.A. DiLeo, M.J. Ganter, M.N. Thone, M.W. Forney, J.W. Staub, R.E. Rogers, B.J. Landi, Balanced approach to safety of high capacity silicon-germanium-carbon nanotube free-standing lithium ion battery anodes, Nano Energy 2 (2013) 268–275.

[43] J.S. Pena, I. Sandu, O. Joubert, F.S. Pascual, C.O. Arean, T. Brousse, Electrochemical reaction between lithium and β-quartz $GeO_2$, Electrochem. Solid-State Lett. 7 (2004) A278–A281.

[44] W. Tang, L.L. Liu, Y.S. Zhu, H. Sun, Y.P. Wu, K. Zhu, An aqueous rechargeable lithium battery of excellent rate capability based on a nanocomposite of $MoO_3$ coated with PPy and $LiMn_2O_4$, Energy Environ. Sci. 5 (2012) 6909–6913.

[45] H.L. Liu, T.T. Yu, D.Q. Su, Z.H. Tang, J.H. Zhang, Y.J. Liu, A.H. Yuan, Q.H. Kong, Ultrathin Ni-Al layered double hydroxide nanosheets with enhanced supercapacitor performance, Ceram. Int. 43 (2017) 14395–14400.

[46] D. Ji, H. Zhou, J. Zhang, Y.Y. Dan, H.X. Yang, A.H. Yuan, Facile synthesis of a metal-organic framework-derived $Mn_2O_3$ nanowire coated three-dimensional graphene network for high-performance free-standing supercapacitor electrodes, J. Mater. Chem. A 4 (2016) 9881–9889.

[47] J.S. Pena, I. Sandu, O. Joubert, F.S. Pascual, C.O. Arean, T. Brousse, Electrochemical reaction between lithium and β-quartz $GeO_2$, Electrochem. Solid-State Lett. 7 (2004) A278–A281.

[48] D. Lv, M.L. Gordin, R. Yi, T. Xu, J. Song, Y.B. Jiang, D. Choi, D. Wang, $GeO_x$/reduced graphene oxide composite as an anode for Li-ion batteries: enhanced capacity via reversible utilization of $Li_2O$ along with improved rate performance, Adv. Funct. Mater. 24 (2014) 1059–1066.

[49] H.W. Wang, Z.J. Xu, H.G. Wei, Z.H. Guo, X.F. Wang, One-step preparation of single-crystalline $Fe_2O_3$ particles/graphene composite hydrogels as high performance anode materials for supercapacitors, Nano Energy 7 (2014) 86–96.

[50] D. Ji, H. Zhou, Y.L. Tong, J.P. Wang, M.Z. Zhu, T.H. Chen, A.H. Yuan, Facile fabrication of MOF-derived octahedral CuO wrapped 3D graphene network as binder-free anode for high performance lithium-ion batteries, Chem. Eng. J. 313 (2017) 1623–1632.